

“The Perfect Slope”: A new robust low-scatter X-ray mass indicator for clusters of galaxies

Alexey Vikhlinin, Andrey V. Kravtsov, Daisuke Nagai
Harvard-Smithsonian Center for Astrophysics
The University of Chicago
Caltech



This presentation is a Moriond version of our recent paper (Kravtsov, Vikhlinin & Nagai¹) where we discussed X-ray proxies for the total cluster mass, including the spectral temperature (T_x), gas mass measured within r_{500} (M_g), and the new proxy, Y_x , which is a simple product of T_x and M_g . We use mock *Chandra* images constructed for a sample of clusters simulated with high resolution in the concordance Λ CDM cosmology. The simulated clusters exhibit tight correlations between the considered observables and total mass. The normalizations of the $M_{500} - T_x$, $M_g - T_x$, and $M_{500} - Y_x$ relations agree to better than $\approx 10 - 15\%$ with the current observational measurements of these relations. Our results show that Y_x is the best mass proxy with a remarkably low scatter of only $\approx 5 - 7\%$ in M_{500} for a fixed Y_x , at both low and high redshifts and regardless of whether clusters are relaxed or not. In addition, we show that redshift evolution of the $Y_x - M_{500}$ relation is close to the self-similar prediction, which makes Y_x a very attractive mass indicator for measurements of the cluster mass function from X-ray selected samples.

1 Introduction

The evolution of the cluster abundance is one of the most sensitive probes of cosmology. The potential and importance of this method have motivated efforts to construct several large surveys of high-redshift clusters during the next several years. However, in order to realize the full statistical power of the upcoming cluster surveys, it is paramount that the relation between cluster mass and observables and any potential biases are well known.

Several cluster observables based on the galaxy velocities, optical light, X-ray observables such as luminosity, temperature, mass of the intracluster medium (ICM), and Sunyaev-Zel'dovich flux have been proposed as proxies of the total cluster mass (see a recent review by Voit²). In this study we focus on the mass indicators derived from cluster X-ray observables.

X-ray luminosity is the most straightforward mass indicator to measure observationally. However, L_x is also the least accurate (internally) of all proposed X-ray proxies for M_{tot} with a large scatter^{3,4} and deviations of the slope of the $L_x - M$ relation from the self-similar prediction⁵. The most common choice of mass proxy in the cluster cosmological studies has been the X-ray temperature of the intracluster gas^{6,7,8,9}. The scatter in the $M - T_x$ relation is smaller compared to that in the $L_x - M$ relation (the upper limit from observations is $\approx 15\%$ in M for fixed T for relaxed clusters¹⁰). In general, existence of a tight relation such as $M - T_x$ indicates that clusters are regular population of objects with their global properties tightly related to total mass, and scatter caused by secondary effects such as substructure in the ICM, non-gravitational processes, and mergers¹¹. More recently, gas mass was used as a proxy for

M_{tot} ^{12,13}. The practical advantage of M_g over T_x is that it can be measured from the X-ray imaging alone. Also, M_g can be expected to be less sensitive to mergers which should translate into smaller scatter in the $M_g - M$ relation. The caveat is that trend of gas mass with cluster mass and evolution with redshift are not yet fully understood.

The use of clusters as efficient probes for precision cosmology puts stringent requirements on observable cluster mass proxies: 1) tight, low-scatter correlation between the proxy and mass, with the scatter insensitive to mergers etc., and 2) simple power-law relation and evolution which can be described by a small number of parameters and be as close as possible to the prediction of the self-similar model. The last point is crucial to ensure that the self-calibration strategies for analyses of large cluster surveys^{14,15,16,17,18} are successful. This is because self-calibration is powerful when cluster scaling relations and their evolution have a simple form which can be parameterized with a small number of parameters.

In general, a mass proxy does not have to be a single cluster property, such as L_x , T_x or M_g . Any physically-motivated combination of these variables that is expected to be tightly related to cluster mass can be used to construct a valid mass indicator. A hint for a better X-ray mass proxy is provided by recent studies based on cosmological simulations of cluster formation^{19,20}, which show that integrated SZ flux, Y_{SZ} is a good, robust mass indicator with low scatter in the $Y_{\text{SZ}} - M$ relation, regardless of the dynamical state of the cluster. In addition, the $Y_{\text{SZ}} - M$ relation exhibits a simple, nearly self-similar evolution with redshift^{21,20}. The physical reason for the robustness of the SZ flux is straightforward: Y_{SZ} is directly related to the total thermal energy of the ICM and thus to the depth of the cluster potential well.

Here we show that a similar robust, low-scatter mass indicator can be constructed using X-ray observables. The indicator, which is simply the product of the X-ray derived gas mass and average temperature, $Y_x = M_g T_x$, correlates strongly with cluster mass with only $\approx 5 - 8\%$ intrinsic scatter. The $Y_x - M_{\text{tot}}$ relation is robust to mergers, in the sense that even for disturbed unrelaxed systems it gives unbiased estimates of mass with the statistical uncertainty similar to that for relaxed systems. In addition, we show that evolution of the slope and normalization of the $Y_x - M$ relation is nearly self-similar. These properties make Y_x particularly useful for measurements of cluster mass function using X-ray surveys.

2 Mass Proxies

Physical properties of virialized systems, such as clusters, are expected to correlate with their total mass. For example, in the self-similar model²² the cluster gas mass is expected to be simply proportional to the total mass, $M_{\Delta_c} = C_{M_g} M_{g,\Delta_c}$, where masses are determined within a radius enclosing a certain overdensity Δ_c with respect to the critical density of the universe at the epoch of observation, $\rho_{\text{crit}}(z)$, and C_{M_g} is a constant independent of cluster mass and redshift. The self-similar relation between cluster mass and temperature is $E(z) M_{\Delta_c} = C_T T^{3/2}$. Here the function $E(z) \equiv H(z)/H_0$ for a flat cosmology with the cosmological constant assumed throughout this study is given by $E(z) = (\Omega_M(1+z)^3 + \Omega_\Lambda)^{1/2}$.

The SZ flux integrated within a certain radius, Y_{SZ} , is proportional to the total thermal energy of the ICM gas and thus to the overall cluster potential, which makes it relatively insensitive to the details of the ICM physics and merging. Y_{SZ} is proportional to the ICM mass and gas mass-weighted mean temperature, $Y_{\text{SZ}} \propto M_{g,\Delta_c} T_m$. The self-similar prediction for the $Y_{\text{SZ}} - M$ relation is

$$E(z)^{2/5} M_{\Delta_c} = C_{Y_{\text{SZ}}} Y_{\text{SZ}}^{3/5}. \quad (1)$$

Cosmological simulations show that Y_{SZ} is a good, low-scatter cluster mass proxy and that $Y_{\text{SZ}} - M$ relation form and evolution are close to the self-similar prediction^{21,23,20}. Given the good qualities of Y_{SZ} as a mass proxy, it is interesting whether a similar indicator can be

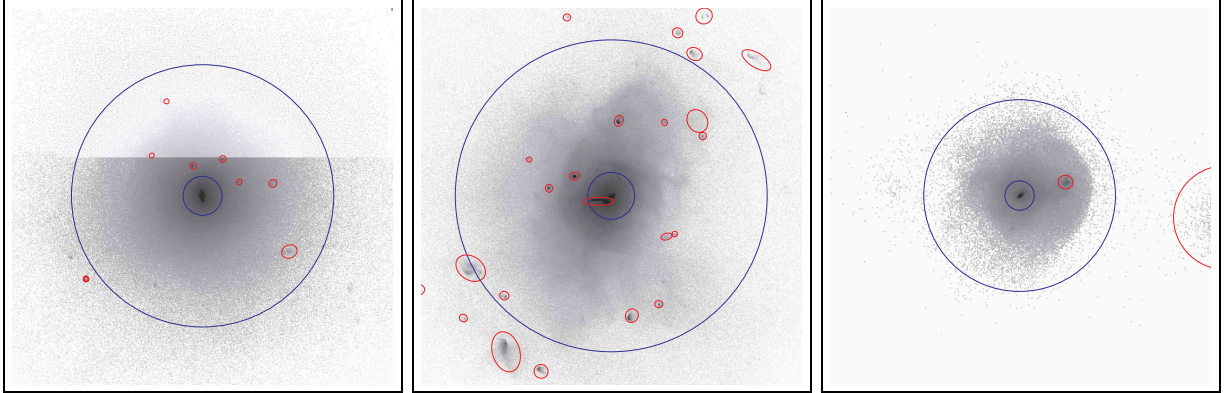


Figure 1: Examples of mock *Chandra* images of our simulated clusters. Small ellipses show substructures detected by our automated software on the mock 100 ksec images. Large circles show the radii $r = r_{500}$ and $0.15 r_{500}$.

constructed from the X-ray observables, which could be used in studies of the X-ray cluster abundances. The simplest X-ray analog of Y_{SZ} is

$$Y_x = M_{g,\Delta_c} T_x, \quad (2)$$

where M_{g,Δ_c} is the gas mass derived from the X-ray imaging data (it is measured within a radius enclosing overdensity Δ_c), and T_x is the mean X-ray spectral temperature. T_x is measured excluding the central cluster region, which can be achieved with moderate angular resolution X-ray telescopes ($\leq 15''$ FWHM). To excise the central regions is desirable because the observed cluster temperature profiles show a greater degree of similarity outside the core¹⁰, and also because this makes the spectral temperature closer to the gas mass averaged T_m .

3 Mock *Chandra* Images and Analyses of Simulated Clusters

To test the quality of T_X , M_g , and Y_X as the total mass proxies, we take the following approach. We use the output of the high-resolution cosmological simulations of clusters in a wide mass range to predict their X-ray emission maps. These maps are convolved with the response of the *Chandra* telescope to create realistic mock “observations” of these clusters. The mock data are used as an input to the actual X-ray data analysis pipeline and measure the proxies (T_X , M_g , and Y_X) as they would be derived by observers.

The simulations and analysis procedure is fully described in Kravtsov et al.¹ The cosmological simulations accurately follow the cluster growth from initial conditions using Adaptive Refinement Tree (ART) N -body+gasdynamics code²⁴, a Eulerian code that reaches the high dynamic range required to resolve cores of mass halos. The peak formal resolution achieved in these simulations, $\approx 3.66 h^{-1}$ kpc, is sufficient to resolve halos of individual galaxies and to follow not only dissipationless dynamics of dark matter and gasdynamics of the ICM, but also star formation, metal enrichment and thermal feedback due to the supernovae type II and type Ia, self-consistent advection of metals, metallicity dependent radiative cooling and UV heating due to cosmological ionizing background.

Generation and analysis of the mock X-ray data reproduces all the effects associated with the *Chandra* response and reconstruction of the 3D ICM properties from the observed projected X-ray spectra. The only exception is that we ignore complications present in reduction of the real *Chandra* data related to background subtraction and spatial variations of the effective area (i.e., we assume that accurate corrections for these effects can be applied to the real data and any associated uncertainties are included in the reported measurement errors).

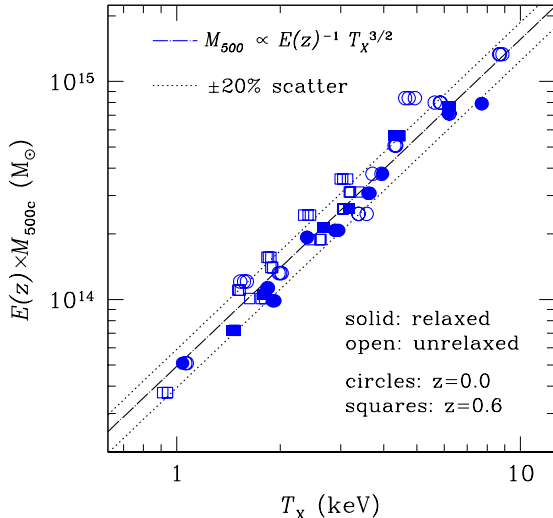


Figure 2: Relation between the X-ray spectral temperature, T_x , and total mass, M_{500} . Separate symbols indicate relaxed and unrelaxed clusters, and also $z = 0$ and $z = 0.6$ samples. The dashed line shows the power law relation with the self-similar slope fit to the entire sample, and the dotted lines indicate 20% scatter.

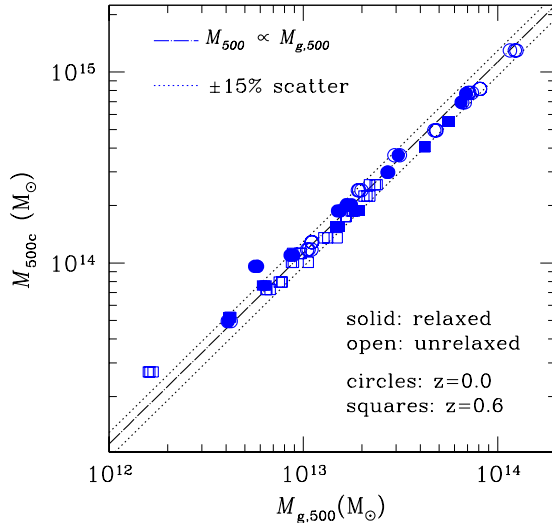


Figure 3: Correlation between gas mass and total mass of the clusters. Both masses are measured within r_{500} . The meaning of the symbols and lines is the same as in Fig. 2. The dotted lines indicate 15% scatter.

Our simulations include clusters in a wide range of mass and dynamical state. We use simulation outputs at redshifts $z = 0$ and $z = 0.6$ to test the evolution in the mass vs. proxy relations. Examples of the mock *Chandra* images are shown in Fig.1.

4 Comparison of Mass Indicators

Figure 2 shows that the slope and evolution of the $M_{500} - T_x$ relation^a are quite close to the self-similar model. There is a $\sim 20\%$ scatter in M_{500} around the mean relation and much of the scatter is due to unrelaxed clusters. Note also that the normalizations of the $M_{500} - T_x$ relation for relaxed and unrelaxed systems are somewhat different: unrelaxed clusters have lower temperatures for a given mass. This may seem counter-intuitive at first, given that one can expect that shocks can boost the ICM temperature during mergers. However, in practice the effect of shocks is relatively small¹¹. The main source of the bias is that during advanced mergers the mass of the system already increased but only a fraction of the kinetic energy of merging systems is converted into the thermal energy of the ICM²⁵.

The $M_{500} - M_g$ relation (Fig. 3) has a somewhat smaller scatter ($\approx 10 - 12\%$) around the best fit power law relation than the $M_{500} - T_x$, but its slope is significantly different from the self-similar prediction — we find $M_{500} \propto M_g^{0.88 \div 0.92}$ compared to the expected $M_{500} \propto M_g$. This is due to the trend of gas fraction with cluster mass, $f_{\text{gas}} \equiv M_g/M_{500} \propto M_{500}^{0.1 \div 0.2}$ present for both the simulated clusters in our sample²⁶ and for the observed clusters¹⁰. The normalization of the $M_{500} - M_g$ relation evolves only weakly between $z = 0.6$ and $z = 0$ (yet, the evolution is statistically significant and it reflects slow evolution of the gas fraction with time²⁶).

The $M_{500} - Y_x$ relation (Fig. 4) has the smallest scatter of only $\approx 5 - 7\%$. Note that this value of scatter includes clusters at both low and high-redshifts and both relaxed and unrelaxed systems. In fact, the scatter in $M_{500} - Y_x$ for relaxed and unrelaxed systems is indistinguishable within the errors. Note also that the figures include points corresponding to the three projections

^aHereafter, M_{500} is the total mass within the sphere corresponding to the mean overdensity of 500 relative to the critical density at the cluster redshift.

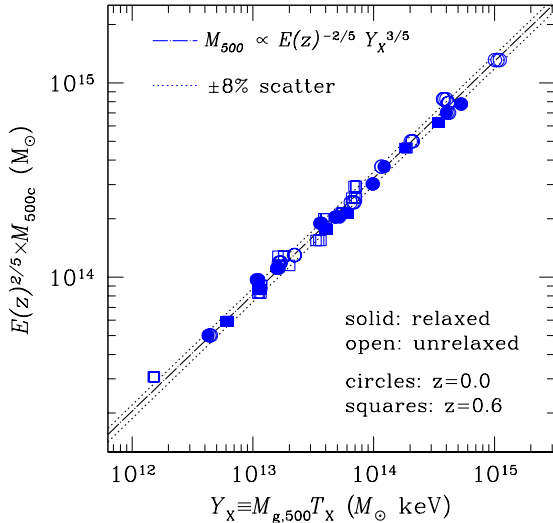


Figure 4: $Y_x - M_{500}$ correlation. The meaning of the symbols and lines is the same as in Fig. 2. The dotted lines indicate 8% scatter.

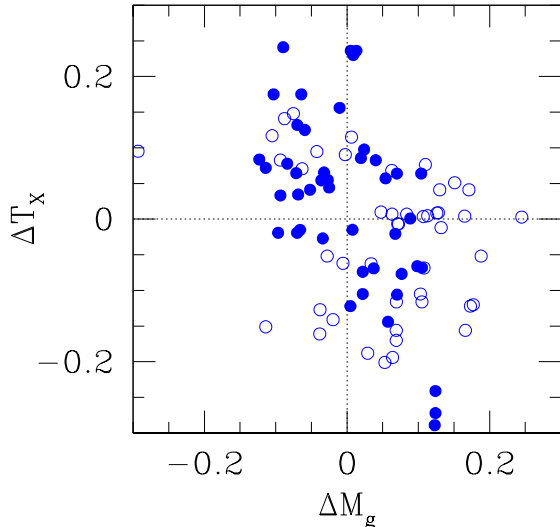


Figure 5: Fractional deviations in T_x and M_g for fixed M_{tot} from their self-similar relations. Solid and open circles show clusters at $z = 0$ and $z = 0.6$, respectively. The deviations for M_g and T_x are generally anti-correlated. A similar anti-correlation exists in the trend with redshift.

of each cluster. Figure 4 shows that the dispersion in the projected values of Y_x for each given cluster is very small, which means that Y_x is not very sensitive to the asphericity of clusters. Remarkably, the scatter of the $M_{500} - Y_x$ relation, which involves direct X-ray observables, is as small as that in the $M_{500} - Y_{\text{SZ}}$ relation ($\approx 7\%$ for our sample).

The comparison of the mass proxies, clearly shows that Y_x , the product of gas mass and X-ray spectral temperature, is more robust and self-similar mass indicator than either of these X-ray observables. Why is the product better than its parts? The answer is obvious from Figure 5 where we show the residuals of temperature and gas mass from their respective relations with total mass. Figure 5 shows that the clusters with temperatures lower than the mean temperature for a given total mass tend to have gas mass higher than the mean, and vice versa. Note also that there is some redshift evolution between $z = 0$ and $z = 0.6$ — more clusters have negative deviations of temperature and positive deviations of measured gas mass at $z = 0.6$ compared to $z = 0$. This redshift evolution is thus in the opposite direction for the gas mass and temperature deviation. The measured M_g systematically increases at higher z for a fixed total mass because high- z clusters are less relaxed on average. For unrelaxed clusters, the ICM density distribution is non-uniform which results in overestimation of M_g from the X-ray data²⁷. Some of the decrease of M_g at lower z may be due to continuing cooling of the ICM which decreases the mass of hot, X-ray emitting gas. The anti-correlation of residuals and opposite evolution with redshift for gas mass and temperature is the reason why the behavior of their product, on average, has smaller scatter and is closer to the self-similar expectation in both the slope and evolution.

5 Discussion and Conclusions

We presented comparison of several X-ray proxies for the cluster mass — the spectral temperature T_x and gas mass M_g derived from the X-ray data within r_{500} , and the new proxy, Y_x , defined as a simple product of T_x and M_g . Analogously to the integrated Sunyaev-Zel’dovich flux, Y_x is related to the total thermal energy of the ICM. To test these mass proxies, we use mock *Chandra* “observations” of a sample of clusters simulated in the concordance Λ CDM cosmology.

The main result of this study is that Y_x is a robust mass indicator with remarkably low scatter of only $\approx 5 - 7\%$ in M_{500} for fixed Y_x , regardless of whether the clusters are relaxed or not. In addition, the redshift evolution of the $Y_x - M_{500}$ relation is close to the self-similar prediction given by equation 1, which makes this indicator a very attractive observable for studies of cluster mass function with the X-ray selected samples.

The $T_x - M_{500}$ relation has the largest scatter ($\approx 20\%$), most of which is due to unrelaxed clusters. The unrelaxed clusters have temperatures biased low for a given mass because a certain fraction of the kinetic energy of merging systems is still in the form of bulk motions of the ICM. The $M_g - M_{500}$ relation shows an intermediate level of scatter, $\approx 10 - 12\%$. This relation does not appear to be sensitive to mergers. It does, however, exhibit significant deviations from self-similarity in its slope, which is due to the dependence of gas fraction within r_{500} on the cluster mass²⁶ (a similar dependence exists for the observed clusters¹⁰).

Generally, all the observable–mass relations we tested demonstrate a remarkable degree of regularity of galaxy clusters as a population. T_x , M_g , and Y_x all exhibit correlations with M_{500} which are close to the expectation of the self-similar model, both in their slope and evolution with time, within the uncertainties provided by our sample. The only exception is the slope of the $M_g - M_{500}$ relation.

Given that our analysis relies on cosmological simulations, it is reasonable to ask whether the simulated clusters are realistic. Although simulations certainly do not reproduce all of the observed properties of clusters, especially in their core regions, the ICM properties outside the core in simulations and observations agree quite well. We illustrate this in Fig. 6, which shows that the $M_g - T_x$ relations for simulated and observed clusters¹⁰. Clearly, both simulated and observed clusters exhibit tight correlations between M_g and T_x which agree remarkably in their slope ($M_g \propto T_x^{1.75}$) and normalization. The normalizations derived from simulated and real clusters agree to $\approx 10\%$, while slopes are indistinguishable and both deviate significantly from the expected self-similar value of 1.5. This is a consequence of significant trends in the gas fraction with cluster mass, $M_g/M_{500} \propto M_{500}^{0.2 \div 0.25}$ for both simulated²⁶ and observed clusters¹⁰. The deviations from the self-similar model also manifest themselves in the absence of any noticeable evolution with redshift^b. Interestingly, the real clusters show a similarly weak evolution in the $M_g - T_x$ relation²⁸. Figure 5 shows that the likely explanation is that the clusters at $z = 0.6$ tend to be colder for the fixed M_{tot} but have higher estimated M_g than their counterparts at $z = 0$ because they are less relaxed.

A similar level of agreement between the simulations and latest *Chandra* measurements exists also for the total mass vs. temperature relation, $M_{500} - T_x$. In fact, the normalization for our simulated sample agrees with the observational results¹⁰ to $\approx 10\%$. This is a considerable improvement over the situation of just several years ago when there was $\approx 30 - 50\%$ discrepancy between observational measurements and cosmological simulations^{29,30}. The $M - T_x$ normalization was revised both in simulations and observations due to (1) inclusion of more realistic physics in cosmological simulations (e.g., radiative cooling and star formation,^{31,32} (2) improved analyses of observed clusters using more realistic gas density profiles^{33,10}, (3) more reliable measurements of the cluster temperature profiles^{34,35,10}, and (4) the use of uniform definition of T_x in observations and in simulations analyses^{36,37,38}. The remaining systematic 10% difference observed at present is likely caused by non-thermal pressure support from bulk gas motions^{39,40,41}, which is unaccounted for by the X-ray hydrostatic mass estimates. In Figure 7 we compare the $Y_x - M_{500}$ relation for the simulated clusters and for the *Chandra* sample¹⁰. The observed clusters show a tight correlation with the slope close to the self-similar value. There is $\approx 15\%$ difference in normalization, likely explained also by neglecting the turbulent pressure support in the *Chandra* hydrostatic mass estimates. The excellent agreement of

^bNote that M_g in Fig.6 is not multiplied by the $E(z)$ factor unlike the total mass in Fig.2 and 4.

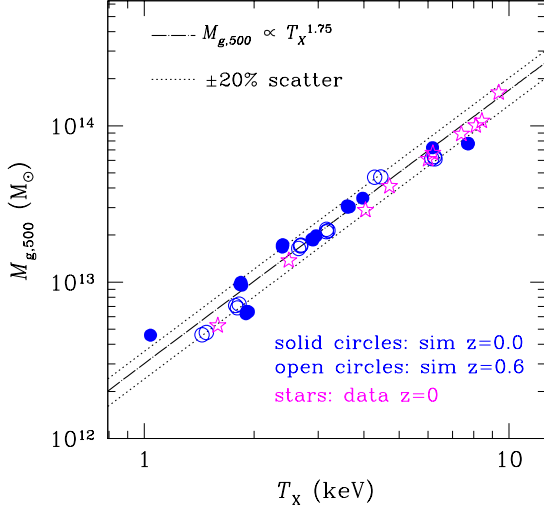


Figure 6: Relation between X-ray spectral temperature and gas mass for the relaxed subsample of simulated clusters (circles) and for a sample of relaxed *Chandra* clusters (stars). Both gas mass and temperature are the quantities derived from analysis of real and mock X-ray data. The error bars in the *Chandra* measurements are comparable to the symbol size and are not shown for clarity. The *dashed line* shows the best fit power law relation with the slope 1.75.

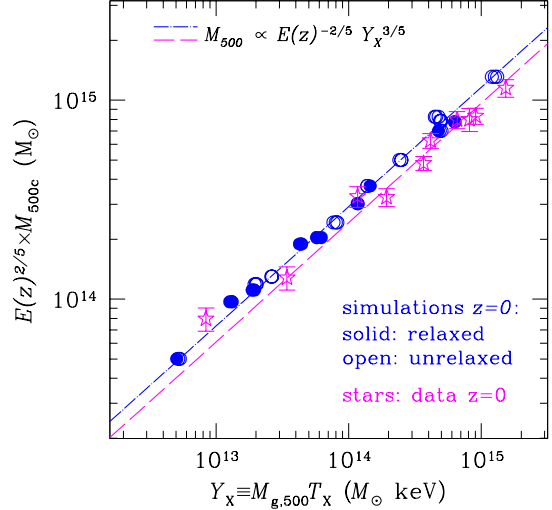


Figure 7: $Y_x - M_{500}$ relation for the $z = 0$ sample of the simulated clusters (circles) and for a sample of relaxed *Chandra* clusters (stars). The gas masses for the simulated clusters are appropriately rescaled (see caption to Fig.6). The *dot-dashed line* shows the best fit power law relation for the simulated clusters with the slope fixed to the self-similar value of $3/5$. The *dashed line* shows the same best fit power law, but with the normalization scaled down by 15%.

simulations and observations in terms of the relation between the two X-ray observables used to compute Y_x ($M_g - T_x$) and a relatively good agreement in the $T_x - M_{500}$ and $Y_x - M_{500}$ relations, gives us confidence that the results presented here are sufficiently realistic.

Our results show that Y_x is clearly most robust and most self-similar X-ray cluster mass indicator. The biases existing in mass estimates based on M_g and T_x anti-correlate both for a given redshift and in terms of evolutionary trends (see Figure 5). This explains why their product, Y_x , is a better mass indicator than T_x and M_g individually. The quality of Y_x compares well to that for the actual three-dimension integral of the ICM thermal energy (proportional to Y_{SZ}) in terms of its low scatter and self-similarity. Y_x may prove to be an even better mass proxy than Y_{SZ} , given that we use ideal 3D measurement of the latter while reproducing the actual data analysis for the former. Note also that Y_{SZ} is more sensitive to the outskirts of clusters, because it involves gas mass-weighted temperature (as opposed to the spectral temperature more sensitive to the inner regions), and thus should be more prone to projection effects.

Note that Y_x is also an attractive mass proxy from the data analysis point of view. First, it reduces observational statistical noise by combining the two independently measured quantities, M_g and T_x , into a single quantity. For example, a 10% measurement uncertainty in T_x translates into a $\sim 15\%$ mass uncertainty through the $M - T_x$ relation and only 6% uncertainty through the $Y_x - M$ relation. Y_x is also less sensitive to any errors in the absolute calibration of the X-ray telescope because the biases in the derived T_x and M_g tend to anticorrelate.

The robustness and low scatter make Y_x an excellent mass indicator for observational measurements of cluster mass function at both $z = 0$ and higher redshifts. The necessary data — an X-ray brightness profile and a wide-beam spectrum excluding the core — are easily obtained with sufficiently deep observations with *Chandra*, *XMM-Newton*, and *Suzaku* (for low-redshift clusters). The small scatter and simple, nearly self-similar evolution of the $Y_x - M$ relation hold promise for the self-calibration strategies for future large X-ray cluster surveys.

This project was supported by the NSF under grants No. AST-0206216 and AST-0239759, and by NASA through grants NAG5-13274 & NAG5-9217 and contract NAS8-39073. D.N. is supported by a Sherman Fairchild postdoctoral fellowship at Caltech. Last but not least, we would like to thank the organizers of the XLIst *Rencontres du Moriond*.

1. A. V. Kravtsov, A. Vikhlinin, and D. Nagai. *ApJ*, in press (*astro-ph/0603205*).
2. G. M. Voit. *Reviews of Modern Physics*, 77:207, 2005.
3. L. David, A. Slyz, C. Jones, W. Forman, S. Vrtilek, and K. Arnaud. *ApJ*, 412:479, 1993.
4. R. Stanek, A. E. Evrard, H. Böhringer, P. Schuecker, and B. Nord. *ApJ submitted (astro-ph/0602324)*, 2006.
5. S. W. Allen, R. W. Schmidt, A. C. Fabian, and H. Ebeling. *MNRAS*, 342:287, 2003.
6. J. P. Henry and K. A. Arnaud. *ApJ*, 372:410, 1991.
7. J. Oukbir and A. Blanchard. *A&A*, 262:L21, 1992.
8. M. Markevitch. *ApJ*, 504:27, 1998.
9. Y. Ikebe, T. Reiprich, H. Böhringer, Y. Tanaka, and T. Kitayama. *A&A*, 383:773, 2002.
10. A. Vikhlinin, A.V. Kravtsov, W. Forman, C. Jones, M. Markevitch, S.S. Murray, and L. Van Speybroeck. *ApJ*, 640:691, 2006.
11. T. B. O'Hara, J. J. Mohr, J. J. Bialek, and A. E. Evrard. *ApJ*, 639:64, 2006.
12. A. Vikhlinin et al. *ApJ*, 590:15, 2003.
13. A. Voevodkin and A. Vikhlinin. *ApJ*, 601:610, 2004.
14. E. S. Levine, A. E. Schulz, and M. White. *ApJ*, 577:569, 2002.
15. W. Hu. *Phys. Rev. D*, 67(8):081304, 2003.
16. S. Majumdar and J. J. Mohr. *ApJ*, 585:603, 2003.
17. M. Lima and W. Hu. *Phys. Rev. D*, 72(4):043006, 2005.
18. S. Wang, J. Khoury, Z. Haiman, and M. May. *Phys. Rev. D*, 70(12):123008, 2004.
19. P. M. Motl, E. J. Hallman, J. O. Burns, and M. L. Norman. *ApJ*, 623:L63, 2005.
20. D. Nagai. *ApJ submitted (astro-ph/0512208)*, 2006.
21. A. C. da Silva, S. T. Kay, A. R. Liddle, and P. A. Thomas. *MNRAS*, 348:1401, 2004.
22. N. Kaiser. *MNRAS*, 222:323, 1986.
23. E. J. Hallman, P. M. Motl, J. O. Burns, and M. L. Norman. *ApJ submitted (astro-ph/0509460)*, 2006.
24. A. V. Kravtsov, A. Klypin, and Y. Hoffman. *ApJ*, 571:563, 2002.
25. B. F. Mathiesen and A. E. Evrard. *ApJ*, 546:100, 2001.
26. A. V. Kravtsov, D. Nagai, and A. A. Vikhlinin. *ApJ*, 625:588, 2005.
27. B. Mathiesen, A. E. Evrard, and J. J. Mohr. *ApJ*, 520:L21, 1999.
28. A. Vikhlinin, L. VanSpeybroeck, M. Markevitch, W. R. Forman, and L. Grego. *ApJ*, 578:L107, 2002.
29. A. Finoguenov, T. H. Reiprich, and H. Böhringer. *A&A*, 368:749, 2001.
30. E. Pierpaoli, S. Borgani, D. Scott, and M. White. *MNRAS*, 342:163, 2003.
31. R. Davé, N. Katz, and D. H. Weinberg. *ApJ*, 579:23, 2002.
32. O. Muanwong, P. A. Thomas, S. T. Kay, and F. R. Pearce. *MNRAS*, 336:527, 2002.
33. S. Borgani et al. *MNRAS*, 348:1078–1096, 2004.
34. M. Markevitch, W. R. Forman, C. L. Sarazin, and A. Vikhlinin. *ApJ*, 503:77, 1998.
35. M. Arnaud, E. Pointecouteau, and G. W. Pratt. *A&A*, 441:893, 2005.
36. P. Mazzotta, E. Rasia, L. Moscardini, and G. Tormen. *MNRAS*, 354:10, 2004.
37. E. Rasia, P. Mazzotta, S. Borgani, L. Moscardini, K. Dolag, G. Tormen, A. Diaferio, and G. Murante. *ApJ*, 618:L1, 2005.
38. A. Vikhlinin. *ApJ*, 640:710, 2006.
39. A. Faltenbacher, A. V. Kravtsov, D. Nagai, and S. Gottlöber. *MNRAS*, 358:139, 2005.
40. E. Rasia et al. *astro-ph/0602434*, 2006.

41. E. Lau, A. V. Kravtsov, and D. Nagai. *ApJ in preparation*, 2006.